International Journal of Innovation in Mechanical Engineering and Advanced Materials
Homepage: publikasi.mercubuana.ac.id/index.php/ijimeam
Vol. 8 (No. 2), 2026, pp. 79-101
DOI: 10.22441/ijimeam.v8i2.38913

Article

Effect of Natural Gas Composition on Thermal Performance and NOx Emission Characteristics in Boiler Combustion Systems

Alrafly Rizky Putra Henryansyah *, A. Grummy Wailanduw, and Mohammad Effendy

Department of Mechanical Engineering, State University of Surabaya, Surabaya 60213, Indonesia
*Corresponding Author: alraflyrizky17@gmail.com (ARPH)

Abstract

The composition of natural gas supplied to industrial boilers varies significantly depending on source origin and upstream processing, particularly in the proportions of heavier alkane fractions (C_2–C_6), nitrogen (N_2), and carbon dioxide (CO_2). While prior studies have predominantly treated fuel composition as a fixed parameter or post-combustion control technologies, the systematic influence of multi-component natural gas composition specifically the C_2+alkane fraction distribution on combustion thermal performance and NO_x formation in medium-capacity industrial boilers remains insufficiently characterized. This study addresses this gap through computational fluid dynamics (CFD) simulations of a 17 ton/hour steam boiler under fifteen systematically designed fuel composition scenarios, maintaining a constant heat input of 11,704 kW and an excess air ratio of 16% across all cases. Simulations were performed using Ansys Fluent 2022 with the shear stress transport k-ω turbulence model, Eddy Dissipation combustion model, and Discrete Ordinates radiation model. The analyzed parameters include furnace temperature distribution, CO_2 mole fraction in flue gas, and thermal NO_x concentration. Results reveal that fuel composition exerts a near-twofold variation in NO_x emissions, from a minimum of 25.88 ppm (Set 14: 88% CH_4 + 12% C_2–C_5 N_2+CO_2 blend) to a maximum of 51.05 ppm (Set 9: CH_4 + C_2–C_5 blend), representing a 97.3% difference attributable solely to compositional variation under identical thermal load conditions. Field-realistic multi-component compositions (Sets 12–15) consistently yield the lowest NOx emissions (25.88–28.01 ppm), approximately 30–49% lower than simplified laboratory compositions (Sets 1–11: 31.93–51.05 ppm), demonstrating that fuel composition management alone without any hardware modification or flue gas treatment can achieve NO_x reductions comparable to conventional emission control strategies. These findings provide quantitative evidence that natural gas composition is a viable and underutilized primary variable for emission control in industrial boiler operations, with direct implications for fuel procurement specifications and supply chain quality management in manufacturing sectors.

Article Info:
Received: 2 June 2026
Revised: 26 July 2026
Accepted: 31 July 2026
Available online: 17 August 2026

Keywords:
natural gas; combustion; boiler; fuel composition; computational fluid dynamics (CFD)

How to cite:

A. R. P. Henryansyah, A. G. Wailanduw, and M. Effendy, "Effect of natural gas composition on thermal performance and NOx emission characteristics in boiler combustion systems," *Int. J. Innov. Mech. Eng. Adv. Mater.*, vol. 8, no. 2, pp. 79-101, 2026

1. Introduction

Natural gas has emerged as one of the most significant primary energy resources worldwide due to its relatively low carbon intensity compared with conventional fossil fuels. Its utilization provides substantial environmental advantages, including lower CO_2 emissions and reduced atmospheric pollutant formation per unit of generated energy [1]. Nevertheless, global CO_2 emissions continue to increase at an estimated annual rate of 1.1%, corresponding to approximately 410 million additional tons released each year relative to the previous period [2].

In Indonesia, the utilization of natural gas in industrial manufacturing processes and power generation systems has shown continuous growth. Among industrial energy systems, steam boilers represent one of the largest consumers of natural gas, and thermal performance studies of such gas-fired power systems remain an active area of Indonesian engineering research, as exemplified by recent condenser heat-transfer evaluations of a combined-

cycle power plant [33]. However, unlike solid and liquid fuels, pipeline-distributed natural gas does not possess a constant chemical composition. The methane concentration typically varies within the range of 80–95 mol%, accompanied by fluctuating fractions of ethane (C_2H_6), propane (C_3H_8), butane (C_4H_{10}), nitrogen (N_2), and carbon dioxide (CO_2), depending on the gas supply source, processing conditions, and seasonal demand variations. Variations in fuel composition significantly influence the thermophysical and combustion characteristics of natural gas because each constituent exhibits distinct calorific values, reaction kinetics, and flame propagation behavior. Consequently, changes in gas composition can produce measurable variations in flame temperature, stoichiometric air–fuel ratio, combustion stability, and exhaust gas distribution [3]. Even relatively small compositional deviations of only a few mole percent may substantially modify the lower heating value (LHV), stoichiometric air requirement, adiabatic flame temperature, and reaction zone structure. These parameters directly govern the thermal efficiency, heat transfer characteristics, and nitrogen oxide (NO_x) formation mechanisms within the boiler combustion chamber [4].

NO_x formation in gas-fired boilers is primarily controlled by thermal NO_x, which is highly sensitive to high temperatures, oxygen availability, and hot gas residence time. Recent literature by Franco et al. (2024) on gas boilers and blended combustion indicates that fuel composition changes can alter NO_x tendencies, but the effects are not always straightforward [5]. This is because temperature increases may coincide with changes in reaction rates, air ratios, and flame structure. Whereas according to research Wright et al. (2022) CO_2 emissions are more directly tied to the amount of carbon atoms oxidized in the fuel, though their concentration in exhaust gases is still influenced by excess air and dilution from atmospheric nitrogen or inert gases in the fuel [6]. Therefore, LNG analysis for boilers requires an approach that captures the simultaneous relationships between composition, calorific value, temperature, and emissions.

Previous combustion studies have reported inconsistent relationships between fuel composition and NO_x formation. Some researchers observed that increasing heavier hydrocarbon fractions tends to increase flame temperature and consequently intensify thermal NO_x formation due to higher local heat release rates. Research conducted by Zhu et al. (2022) reported that certain multicomponent fuel mixtures may instead produce lower NO_x emissions due to improved heat distribution and reduced localized hot spots inside the combustion chamber [7]. The findings reported by Min et al. (2026) indicate that NO_x behavior cannot be explained solely by heating value differences, but also depends strongly on spatial combustion characteristics, reaction zone distribution, and thermal uniformity within the furnace geometry [8]. These contradictory outcomes suggest that the NO_x response to fuel composition cannot be reduced to LHV differences alone, but is instead mediated by spatial combustion characteristics, reaction zone geometry, and furnace configuration factors that differ substantially between experimental setups. Resolving this contradiction therefore requires a controlled, geometry-specific investigation rather than generalized fuel comparisons.

In addition, most recent CFD investigations focus predominantly on emission reduction technologies such as flue gas recirculation, burner modification, staged combustion, or air distribution optimization. Although these approaches successfully reduce NO_x emissions, fuel composition itself is often treated as a secondary parameter or represented using simplified methane-based assumptions. As a result, the thermodynamic influence of realistic natural gas compositional variability remains inadequately quantified, particularly for industrial boilers operating under constant heat input constraints. Several studies, such as those conducted by Erne et al. (2023) also employed laboratory-scale combustors or domestic boiler systems, which may not accurately represent combustion behavior in medium-scale industrial steam boilers [9]. Consequently, the interaction between heavier hydrocarbon fractions, inert gas dilution, flame temperature distribution, and NO_x formation in practical industrial boiler geometries remains insufficiently characterized. Moreover, studies on the simultaneous interaction of heavy alkane content with NO_x distribution in medium-to-large capacity boilers are rarely published. Many gas combustion studies use methane as a representative fuel, despite operational LNG containing C2+ hydrocarbon fractions that alter combustion characteristics. Conversely, boiler emission research often focuses on control technologies like flue gas recirculation, low- NO_x burners, or reductant injection, without treating fuel composition as the primary variable [10]. Therefore, by Jiang et al. (2026) further research is needed to understand the influence of fuel composition on combustion and emissions in industrial boilers [11].

Based on these limitations, the present study addresses the existing research gap by investigating the influence of realistic natural gas compositional variability on combustion behavior in an industrial steam boiler using CFD simulation. Unlike previous studies that

simplified natural gas as methane-dominated fuel or focused primarily on emission-control technologies, the present work systematically investigates the combustion behavior of realistic multicomponent LNG compositions under constant boiler operating conditions using a medium-scale industrial steam boiler geometry. The study specifically reveals how variations in C2+ hydrocarbon fractions and inert gas dilution simultaneously modify flame temperature distribution, thermal uniformity, and NO_x formation characteristics, which remain insufficiently addressed in previous CFD boiler investigations. The main contribution of this study is to provide a clearer understanding of the interaction between fuel composition, combustion temperature distribution, and NO_x formation mechanisms under representative industrial boiler operating conditions. In addition, the numerical model is validated directly against natural gas commissioning measurement data recorded on the physical boiler unit represented in the CFD geometry, using gas-chromatography verified fuel composition, thereby grounding the simulation results in field measured performance. This understanding is expected to support more accurate fuel-quality assessment, combustion tuning, and emission-control strategies for industrial natural-gas-fired boilers.

2. Methods

This section describes the numerical framework used to simulate combustion in the industrial steam boiler. It first presents the research design and the modelled study object, followed by the governing conservation equations and the turbulence, radiation, and combustion closures. It then defines the combustion reaction and thermal-NO_x mechanisms, the boundary conditions and the fifteen fuel composition scenarios examined, the data-analysis procedure, and the grid-independence study that establishes the mesh resolution used throughout.

2.1. Research design and study object

In this study, numerical modeling was performed using Ansys Fluent 2022, a widely used CFD software package. The analysis is based on the Reynolds-Averaged Navier–Stokes (RANS) equations. The following sections detail the governing equations, turbulence model, combustion model, and chemical kinetic mechanisms employed. This is expressed in Table 1 model specification.

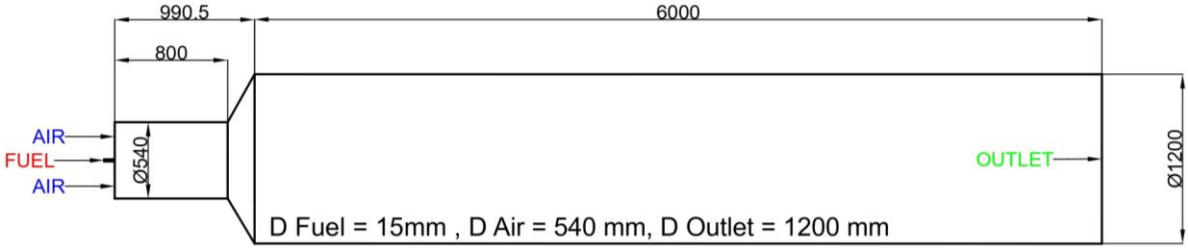

Figure 1. Solved two-dimensional (2D) axisymmetric chamber dimension schematic used for all CFD simulations in this study

Table 1. CFD sub-models and key operating parameters used in the Ansys Fluent 2022 simulations, including the viscous/turbulence closure, radiation model, species-transport and combustion models, soot model, and absorption-coefficient method, together with the assumed equivalence ratio (0.86) and excess air ratio (1.16) and their corresponding literature references.

Model	Description	Reference
Viscous	Standard K-ω	[12]
Radiation	Discrete Ordinates	[13]
Species	Species Transport	[14]
Turbulence Model	Shear Stress Transport	[12]
Combustion Model	Eddy Dissipation Model	[15]
Equivalence Ratio	0.86	[13]
Excess Air	1.16	[13]
Soot	Moss-Brookes	[16]
Absorption Coefficient	WSGGM	[11]

The selection of this boiler type is based on its representativeness in Indonesia's medium-to-large manufacturing industry, where 17 ton per hour boilers are the most common configuration. The modeled burner system is a single diffusion burner with structured primary air flow.

The computational domain was modeled as a two-dimensional (2D) axisymmetric geometry about the burner centerline, exploiting the rotational symmetry of the single circular diffusion burner and cylindrical furnace chamber. Figure 1 shows the 2D axisymmetric dimensioned schematic that was actually solved.

2.2. Governing equations

This section presents the fundamental conservation equations continuity, momentum, energy, and species transport solved within the steady RANS framework [12]. Vector quantities are denoted in bold italic throughout; the operator "·" denotes the vector dot product.

The steady-state continuity equation is written as

$$\nabla.(\rho u) = 0 \tag{1}$$

Refer to Equation (1), where ρ is the fluid density and u is the velocity vector. Because all cases in this study represent converged, time-invariant operating conditions, the unsteady *(∂/∂t)* term of the general continuity equation reduces to zero and is omitted.

The steady RANS momentum equation is obtained from Newton's second law, including the Reynolds-stress term arising from time-averaging the nonlinear convective term:

$$\nabla.(\rho uu) = -\nabla_p + \nabla(\tau - \rho u'u') + \rho g \tag{2}$$

Equation (2), where p is the mean pressure, τ is the viscous stress tensor, and g is the gravitational acceleration vector. The term $-\rho u'u'$ is the Reynolds-stress tensor arising from turbulent fluctuations; it is closed via the Boussinesq eddy-viscosity hypothesis using the turbulent viscosity μ_t predicted by the SST k-ω model (Section 2.3). As with the continuity equation, the unsteady term is zero under the steady-state formulation adopted here.

The steady energy equation, expressed in index notation, accounts for advection, pressure work, viscous dissipation, and net heat flux (conduction, radiation, and turbulent transport):

$$\frac{\partial(\rho u_j h)}{\partial x_j} = \frac{u_j \partial p}{\partial x_j} + \tau_y \left(\frac{\partial U_i}{\partial x_j}\right) - \frac{\partial q}{\partial x_j} \tag{3}$$

In Equation (3), h is the specific enthalpy, τ_{ij} the viscous stress tensor, and q_j the total heat-flux vector, which includes the radiative source term coupled from the Discrete Ordinates (DO) model. Density (ρ) and pressure (p) are notated distinctly throughout this manuscript to avoid ambiguity, and ∂ (partial derivative) is used consistently in place of δ.

Ideal gas equation;

$$p = \rho \frac{R_0}{MW_{mix}} T \tag{4}$$

Equation (4) closes the system by relating the mixture density to the local pressure, temperature, and mean mixture molecular weight (MW_{mix}) under the ideal-gas assumption adopted throughout this study.

The radiation model employs the Discrete Ordinates (DO) method to capture radiative heat transfer. The DO model considers the Radiative Transfer Equation (RTE) for absorbing, emitting, and scattering media. The RTE in the direction s as the field equation is given by the following equation:

$$\nabla.I(\vec{r},\vec{s}')(\vec{s}) + (a+\sigma_s)I(\vec{r},\vec{s}) = an^2\frac{\sigma T^4}{\pi} + \frac{\sigma_s}{4\mu}\int_0^{4\pi} I(\vec{r},\vec{s}')\,\Phi(\vec{s},\vec{s}')d\Omega' \tag{5}$$

In Equation (5) I is the radiation intensity, dependent on position and direction; r is the position vector; s is the direction vector; s is the path length; a is the absorption coefficient; n is the refractive index; σ_s is the scattering coefficient; σ is the Stefan-Boltzmann constant (5.67×10^{-8} W/m^{2}K^4); Ω' is the solid angle; T is the local temperature; and Φ is the phase function.

Since Species Transport is used as the species model (Table 1), the steady mass-fraction transport equation for species i is solved in the form.

$$\nabla.(\rho u Y_i) = \nabla.J_i + R_i \tag{6}$$

where Y_i is the mass fraction of species i, $J_i = -(\rho D_{i,m} + \mu_t/Sc_t)\ \nabla Y_i$ is the diffusion flux of species i (combining laminar and turbulent diffusion), and R_i is the net production rate of species i by chemical reaction, obtained from the Eddy Dissipation combustion model (Section 2.3). This equation is solved simultaneously with the energy equation, with the reaction heat release from R_i entering Equation (3) as a source term.

$$MW_{mix} = \sum y_i MW_i \tag{7}$$

$$w_i = \frac{y_i MW_i}{MW_{mix}} \tag{8}$$

where y_i denotes the mole fraction of the i-th species and MW_i is its corresponding molecular weight in units of kg/kmol. This formulation is derived directly from Dalton's law of partial pressures applied to ideal gas mixtures and is widely adopted in the characterization of natural gas, liquefied petroleum gas (LPG), and biomass-derived synthesis gas (syngas) compositions. The accuracy of MW_{mix} is highly sensitive to the precision of compositional analysis, typically obtained via gas chromatography (GC) or process mass spectrometry. Recent computational studies on variable fuel composition blends have highlighted the importance of dynamic molecular weight updating in real-time combustion control strategies for gas turbines and industrial burners. The molecular weight and lower heating value of each hydrocarbon constituent used in this calculation are listed in Table 2 and Table 3, respectively.

Stoichiometric O_2 requirement equation;

$$C_xH_y + aO_2 \rightarrow xCO_2 + \frac{y}{2}H_2O \tag{9}$$

where the stoichiometric oxygen coefficient is given by $a = x + y/4$, corresponding to the moles of O_2 required per mole of fuel to achieve complete combustion. This expression is obtained by applying atomic conservation of carbon, hydrogen, and oxygen across the reaction. The coefficient a is a function solely of the elemental composition of the fuel and is independent of temperature or pressure under the ideal gas assumption.

Theoretical air requirement;

$$Air = O_2 + 3.76N_2 \tag{10}$$

$$Air_t = Air\ x\ 28.97 \tag{11}$$

In Equation (10) and Equation (11) the coefficient 3.76 represents the nitrogen-to-oxygen molar ratio (79/21 = 3.76) and remains constant for dry air under standard conditions. This simplification neglects minor constituents such as argon and carbon dioxide, whose combined volumetric fraction is approximately 1%, and is widely accepted as sufficient for engineering-level combustion calculations.

The resulting quantity Air_t represents the theoretical air mass (kg) required for complete combustion per kmol of fuel mixture. The value 28.97 kg/kmol is the accepted mean molecular weight of dry air, derived from the weighted average of its major constituents.

Stoichiometric Air-Fuel Ratio (AFR);

$$AFR = \frac{Air_t}{MW_{mix}} \tag{12}$$

Deviations from the stoichiometric AFR are quantified using the equivalence ratio φ or the excess air ratio λ, where $\lambda = 1/\varphi$. Lean combustion ($\lambda > 1$) provides thermodynamic advantages in terms of reduced peak flame temperature and lower NO_x emissions, while rich combustion ($\lambda < 1$) risks incomplete combustion and elevated CO and unburned hydrocarbon (UHC) concentrations. The mixture fraction (f) equation is given in Equation (13) and (14).

Fuel mass flow rate;

$$m_{fuel} = \frac{Q_{in}}{LHV_{mix}} \tag{13}$$

Table 2. Molecular weight of the six hydrocarbon constituents (methane through hexane, C_1–C_6) present in the fuel-composition sets of Table 4, used to compute the mixture molecular weight (MW_{mix}) of each set via Equations (7)-(8).

No	Component	Formula	Molecular Weight	Units
1	Methane	CH_4	16.0428	g/mol
2	Ethane	C_2H_6	30.069	g/mol
3	Propane	C_3H_8	44.0956	g/mol
4	Butane	C_4H_{10}	58.1222	g/mol
5	Pentane	C_5H_{12}	72.1488	g/mol
6	Hexane	C_6H_{14}	86.1754	g/mol

Table 3. Lower heating value (LHV) of the same six hydrocarbon constituents used to compute the mixture LHV of each fuel-composition set (Table 4 and Table 5), with the corresponding literature source for each value.

No	Component	Formula	Lower Heating Value	Units	Reference
1	Methane	CH_4	50	MJ/kg	[17]
2	Ethane	C_2H_6	47.47	MJ/kg	[18]
3	Propane	C_3H_8	44.0956	MJ/kg	[19]
4	Butane	C_4H_{10}	45.73	MJ/kg	[20]
5	Pentane	C_5H_{12}	45.35	MJ/kg	[21]
6	Hexane	C_6H_{14}	44.75	MJ/kg	[22]

Air mass flow rate;

$$m_{air} = AFR\ x\ m_{fuel}\ x\ Excess\ Air \tag{14}$$

The turbulent kinetic energy transport equation of the SST k-ω model (steady form), including the modeled Reynolds-stress production term P_k, is written as:

$$\nabla(\overline{\rho u}k) = \nabla.\left(\left(\mu + \frac{\mu_t}{\sigma_k}\right)\nabla k\right) + P_k - \rho\beta\ k\omega \tag{15}$$

In Equation (15), $P_k = -\rho u'u'/\nabla u$ is the turbulence production term (the Reynolds-stress – mean strain-rate product) and the specific dissipation rate ω is solved through its companion transport equation, blended between the k-ω formulation near walls and the k-ε formulation in the free stream, per the standard SST closure of Menter [12].

2.3. Combustion reaction mechanism

The combustion reaction model used encompasses complete oxidation reactions for each fuel component. The modeled stoichiometric reactions include the combustion of:

Methane

$$CH_4 + 2O_2 \rightarrow CO_2 + 2H_2O \tag{16}$$

Ethane

$$2C_2H_6 + 7O_2 \rightarrow 4CO_2 + 6H_2O \tag{17}$$

Propane

$$C_3H_8 + 5O_2 \rightarrow 3CO_2 + 4H_2O \tag{18}$$

Butane

$$2C_4H_{10} + 13O_2 \rightarrow 8CO_2 + 10H_2O \tag{19}$$

Pentane

$$C_5H_{12} + 8O_2 \rightarrow 5CO_2 + 6H_2O \tag{20}$$

Hexane

$$2C_6H_{14} + 19O_2 \rightarrow 12CO_2 + 14H_2O \quad (21)$$

NO_x formation in this study was modeled exclusively using the thermal (extended Zeldovich) mechanism, coupled with the nitrogen-oxide species transport equation (Equation 6). The two elementary steps solved are

$$N_2 + O \rightarrow NO + N \quad (22)$$

$$N + O_2 \rightarrow NO + O \quad (23)$$

2.4. Boundary conditions

Uniform velocity and uniform temperature of T = 298 K are set at the inlet, while a pressure outlet with p = 1 atm is imposed at the exit of the domain. Consistent with the 2D axisymmetric formulation (Section 2.1), the burner centerline is defined as the axis of symmetry, about which zero radial velocity gradient and zero flux of all variables are imposed; this axis condition is what permits the three-dimensional cylindrical chamber to be represented by the 2D computational domain solved in this study. The external edges of the domain are modeled as symmetry boundaries to take account of the interaction with the flames from the nearby slits: more specifically, we impose zero normal velocity and zero normal gradients of all variables at the symmetry plane. At the fluid-solid interfaces, a no-slip boundary condition is applied for velocity, while no thermal boundary conditions are required as heat fluxes. The variations of natural gas fuel compositions in Table 4 were designed to cover a representative range of real-world supply conditions. All variations maintain a fixed methane (CH_4) fraction of 0.88 mol (88%), reflecting the lower boundary of methane content commonly found in commercial Indonesian natural gas supplies.

Sets 1–11 focus on differences in heavy alkane proportions (C_2H_6, C_3H_8, C_4H_{10}, C_5H_{12}) while keeping the total non-methane fraction at 12 mol%, representing simplified laboratory-style compositions used widely in the combustion literature. Sets 12–15 explore field-realistic multicomponent compositions, formulated using gas-chromatography (GC) verified natural gas composition data obtained from the physical boiler unit modeled in this study (see Section 3.2), with Set 12-15 additionally containing 2.3 mol% nitrogen (N_2) as an inert

Table 4. Fuel composition (mole fraction) of the fifteen simulated natural-gas scenarios, all evaluated at the same constant heat input (11,704 kW) and 16% excess air ratio, with a fixed methane fraction of 0.88 (88 mol%) held constant across every set. Sets 1–11 are simplified laboratory-style blends that vary only the heavy-alkane fractions (C_2H_6–C_5H_{12}) within a 12 mol% non-methane budget, representing compositions commonly used in the combustion literature. Sets 12–15 are field-realistic, gas-chromatography (GC)-verified multicomponent compositions obtained from the physical boiler unit modeled in this study (Section 3.2).

Set	CH_4	C_2H_6	C_3H_8	C_4H_{10}	C_5H_{12}	C_6H_{14}	N_2	CO_2
1	0.88	0.09	0.03	0.00	0.00	0.00	0.00	0.00
2	0.88	0.072	0.048	0.00	0.00	0.00	0.00	0.00
3	0.88	0.096	0.018	0.006	0.00	0.00	0.00	0.00
4	0.88	0.078	0.03	0.012	0.00	0.00	0.00	0.00
5	0.88	0.066	0.042	0.012	0.00	0.00	0.00	0.00
6	0.88	0.072	0.03	0.018	0.00	0.00	0.00	0.00
7	0.88	0.054	0.042	0.024	0.00	0.00	0.00	0.00
8	0.88	0.084	0.024	0.0084	0.0036	0.00	0.00	0.00
9	0.88	0.072	0.03	0.012	0.006	0.00	0.00	0.00
10	0.88	0.072	0.024	0.0144	0.0096	0.00	0.00	0.00
11	0.88	0.06	0.03	0.018	0.012	0.00	0.00	0.00
12	0.88	0.031	0.0208	0.0142	0.0049	0.0025	0.023	0.0237
13	0.88	0.031	0.0208	0.0139	0.0048	0.0024	0.023	0.0241
14	0.88	0.0372	0.0209	0.0142	0.0049	0.0025	0.023	0.0176
15	0.88	0.0312	0.0235	0.014	0.0048	0.0024	0.023	0.02126

Table 5. Calculated lower heating value (LHV), stoichiometric air-fuel ratio (AFR), and the resulting fuel and air mass flow rates required to maintain the constant heat input of 11,704 kW at 16% excess air, for each of the fifteen fuel-composition sets listed in Table 4.

Set	LHV MJ/kg	AFR kg air/fuel	Mass Fuel kg/s	Mass Air kg/s
1	49.364	16.908	0.237094	4.650
2	49.364	16.878	0.23745	4.649
3	49.365	16.908	0.23709	4.650
4	49.265	16.868	0.23757	4.649
5	49.216	16.849	0.23781	4.648
6	49.216	16.849	0.23781	4.648
7	49.121	16.812	0.23827	4.647
8	49.274	16.872	0.23753	4.649
9	49.191	16.840	0.23793	4.648
10	49.152	16.825	0.23812	4.647
11	49.073	16.794	0.2385	4.646
12	49.318	17.086	0.2373154	4.703
13	49.323	17.087	0.2372923	4.703
14	49.297	17.077	0.2374159	4.703
15	49.303	17.075	0.2373903	4.702

component to simulate high-nitrogen natural gas conditions. The detailed compositions are presented in Table 4 composition variation fuel and Table 5 (calculation values).

2.5. Data analysis

Simulation output data was extracted for each radial distance (z) along the combustion chamber length. Average values were calculated as the arithmetic mean of all data points within the simulation domain. Comparisons between sets were conducted descriptively and quantitatively to identify trends and correlations between fuel composition parameters and combustion output variables.

2.6. Grid independence study

Grid independence analysis constitutes an essential validation step in numerical simulations, used to identify an appropriate mesh resolution and to verify that the combustion simulation results remain insensitive to variations in mesh density or refinement level. In this study, a single-tube steam boiler was employed as the reference model, and three mesh configurations coarse, medium, and fine were developed for the grid independence evaluation, with their schematic layout presented in Figure 3. The total number of computational mesh elements varied from 264,299 to 316,451, while the outlet temperature was used as the primary evaluation parameter. Based on the convergence results illustrated in Figure 2, the outlet temperature exhibited convergence at approximately 299,775 cells, indicating that additional mesh refinement produced only insignificant changes in the simulation outcomes. Therefore, the mesh containing 299,775 computational cells was selected as the optimum grid configuration for the subsequent combustion simulations and analyses. Figure 3 (b) presents an enlarged (zoomed-in) view of the mesh detail in the burner region of the same 2D axisymmetric domain shown in Figure 3 (a).

3. Results and Discussion

This section presents and interprets the CFD results for the fifteen fuel-composition scenarios. It first summarizes the overall combustion outputs and validates the model against commissioning measurements, then examines in turn the effect of natural gas composition on furnace temperature distribution, CO_2 concentration, and NO_x emission, followed by the temperature- NO_x relationship. It closes by outlining the principal modeling limitations and the novel findings of the study.

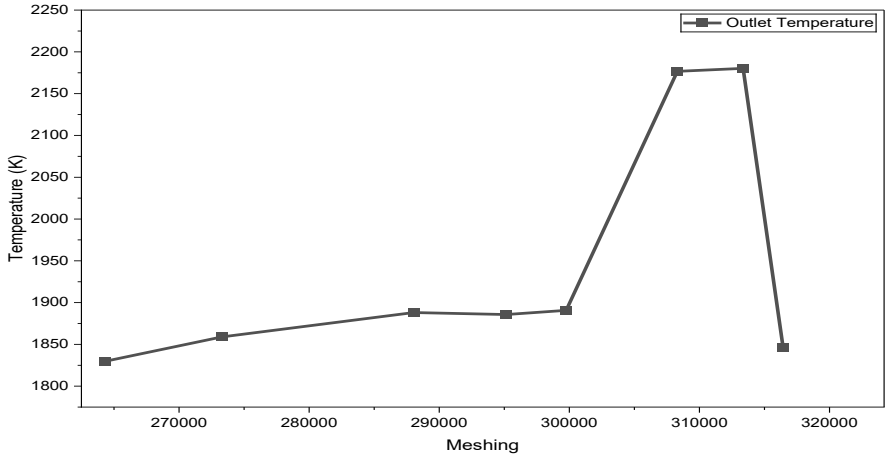

Figure 2. Grid-independence (mesh optimization) study for the 2D axisymmetric boiler domain: variation of the domain-averaged outlet temperature with the number of computational (tetrahedral) mesh elements across three configurations (coarse, medium, and fine; 264,299–316,451 elements), showing convergence at approximately 299,775 elements.

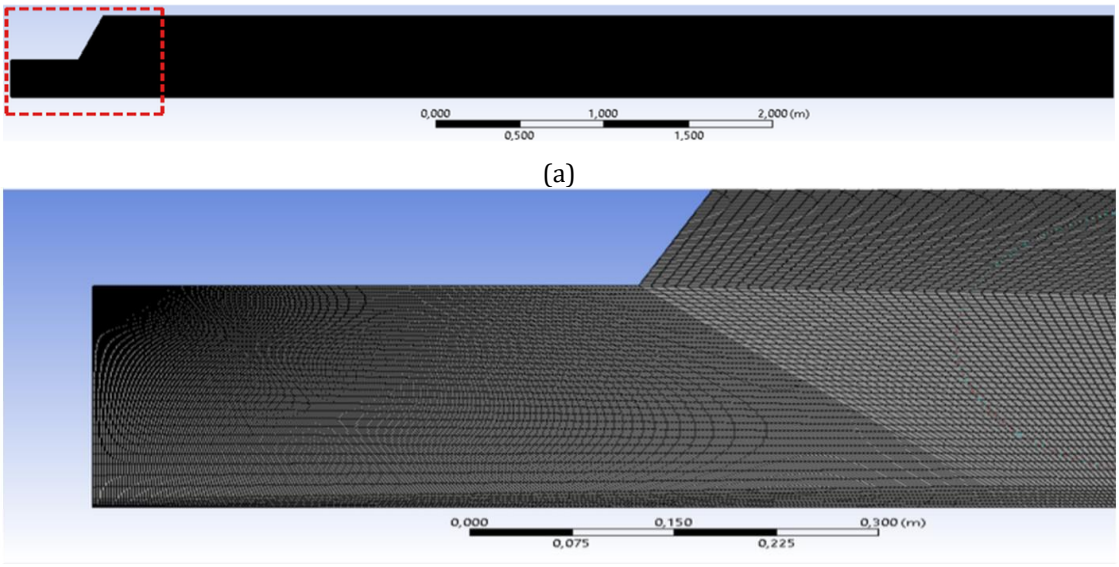

Figure 3. Computational mesh of the two-dimensional (2D) axisymmetric boiler combustion-chamber domain, generated using a tetrahedral mesh with the converged total of 299,775 elements identified (a), Enlarged (zoomed-in) view of the tetrahedral mesh detail in the burner region of the same 2D axisymmetric domain (299,775 elements total) (b).

3.1. Summary of results

All fifteen simulation variations were successfully run to convergence. The complete results are presented in Table 6 below, which summarizes the average and maximum combustion chamber temperatures, average and maximum CO_2 concentrations, and average and maximum NO_x concentrations.

3.2. Model validation

The numerical model was validated against natural-gas commissioning measurement data recorded directly on the physical boiler unit represented in this study (Boiler-2, 17,000 kg/h steam capacity, 16 bar, BOSCH/UL-S 16000, single diffusion burner GKP-1200 M WD_{100}), commissioned on 22 December 2016 and covering ten load positions from 10% to 100% of rated capacity. At each load position, flue-gas CO_2 concentration (dry basis, flue-gas analyzer) was recorded.

Table 6. Summary of CFD results for the fifteen fuel-composition sets defined in Table 4: domain-averaged and maximum combustion-chamber temperature (K), CO_2 mole fraction in the flue gas (%), and thermal NO_x concentration (ppm), all obtained at the constant heat input of 11,704 kW and 16% excess air.

Set	Temperature (K)		CO_2 (mole fraction %)		NO_x (ppm)	
	Avg	Max	Avg	Max	Avg	Max
1	1853.31	2384.90	8.088	9.664	32.29	60.98
2	1856.19	2377.93	8.133	9.708	31.93	60.60
3	1845.91	2373.55	7.963	9.686	32.17	60.72
4	1848.31	2385.67	8.062	9.726	39.51	74.02
5	1849.27	2391.49	8.176	9.747	33.45	64.05
6	1837.99	2397.24	8.154	9.769	34.12	65.10
7	1864.08	2391.48	8.236	9.838	34.46	65.92
8	1852.60	2379.73	8.135	9.715	32.36	61.47
9	1841.76	2390.56	8.083	9.768	51.05	92.66
10	1849.58	2391.07	8.206	9.778	34.19	65.37
11	1845.14	2401.75	8.247	9.821	35.61	68.36
12	1826.02	2335.29	8.258	9.758	26.43	52.13
13	1825.04	2335.69	8.263	9.758	26.43	52.12
14	1855.59	2324.91	8.263	9.790	25.88	50.76
15	1832.66	2347.92	8.296	9.775	28.01	55.41

Table 7. Validation of the CFD-predicted dry-basis flue-gas CO_2 concentration (Sets 12–15, the GC-verified field-realistic compositions) against the commissioning measurement recorded at the boiler's 100% (rated) load operating point.

Parameter	CFD (Dry Basis Equivalent) Set 12-15	Commissioning measurement (100% load)	Deviation
CO_2 (%, dry)	10.40–10.44	10.40	0.27%

Because the CFD simulations were performed at a single fixed operating condition (heat input = 11,704 kW), the corresponding full-load commissioning point was identified by cross-checking the fuel mass flow rate. The CFD-assumed fuel flow rate (0.2373 kg/s = 854 kg/h) corresponds to 1,095–1,139 Nm^3/h at typical pipeline natural-gas density (ρ = 0.75–0.78 kg/Nm^3), which closely matches the measured 100%-load flow rate of 1,122.9 Nm^3/h. This confirms that the CFD-assumed heat input corresponds to the boiler's 100% (rated) load condition, consistent with the boiler's rated steam duty of 17,000 kg/h at 16 bar (11.1–11.7 MW thermal duty at 92–93% efficiency, matching the assumed 11,704 kW heat input). Before this matched operating point could be compared with the CFD results, however, a basis correction was required: CFD species output (Table 6) is inherently reported on a wet basis (including combustion-product H_2O), whereas the flue-gas analyzer measurements are reported on a dry basis (after moisture condensate removal). Direct comparison without basis correction would therefore be invalid. A stoichiometric wet-to-dry conversion follows the same combustion balance already established in Equations (7)–(14) and Equations (16)–(21). Table 7 compares the CFD prediction with the commissioning measurement at this matched 100% load operating point.

The dry-basis CO_2 concentration (10.40–10.44%) shows excellent agreement with the measured value (10.40%), corresponding to a deviation of only 0.27%. This close agreement supports the physical validity of the combustion stoichiometry and species-transport framework adopted in the present model at the boiler's rated operating condition.

To further test the robustness of the combustion-stoichiometry framework underlying the CFD model across the full 10–100% load range, the same GC-verified composition (Sets 12–15) was used to compute theoretical dry-basis CO_2 at each of the ten measured load positions (10–100%). This is a stoichiometric-equilibrium extension of the same combustion framework used by the CFD model; it is reported here as an independent theoretical calculation, not as an additional CFD (Ansys Fluent) simulation, since Fluent was run only at the single 100%-load operating point described above. Table 8 presents this comparison at each of the ten load positions.

Table 8. Theoretical stoichiometric dry-basis CO_2 concentration, computed from the same GC-verified fuel composition (Sets 12–15) using the combustion-stoichiometry framework of Equations (7)-(14) and (16)-(21), compared against the commissioning measurements across the full 10–100% boiler load range.

Load (%)	CO_2 Meas. (%)	CO_2 Theory (%)	Err. CO_2 (%)
10	6.8	6.74	0.84
20	7.6	7.58	0.24
30	8.3	8.25	0.63
40	8.8	8.86	0.69
50	9.1	9.23	1.43
60	9.5	9.61	1.11
70	9.9	10.04	1.42
80	10.1	10.29	1.90
90	10.4	10.55	1.41
100	10.4	10.61	2.00

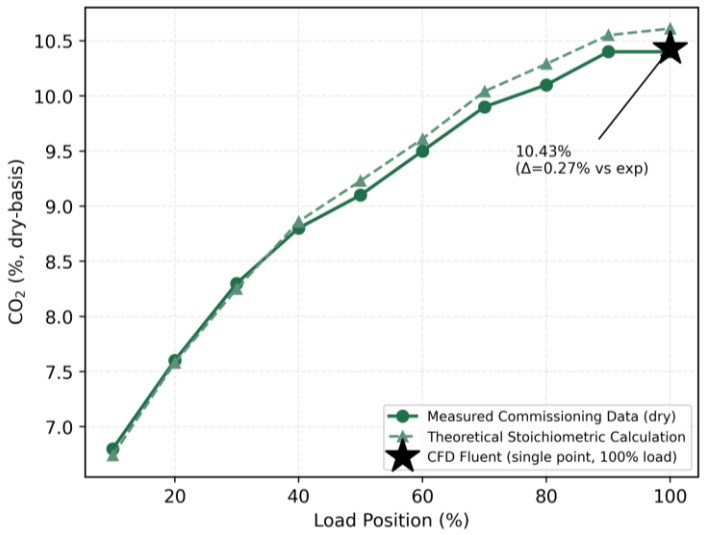

Figure 4. Model validation across the full commissioning load range (10–100% boiler load): measured versus theoretical dry-basis CO_2 concentration (Table 8), computed using the GC-verified fuel composition of Sets 12–15.

Across the full load range, the mean deviation is 1.17% for CO_2, as plotted in Figure 4. The agreement is consistently strong at every load point, confirming that the combustion stoichiometry framework is physically valid for the GC-verified fuel composition across the full operating range of this boiler.

In summary, the close agreement in CO_2 concentration (0.27% deviation at the matched operating point; 1.17% mean deviation across the full load range) and in fuel mass-flow scale supports the physical validity of the combustion and stoichiometric framework adopted in the present model. This validation does not extend to NO_x, as the commissioning report does not include a NO_x measurement (only CO ppm, a different species and formation pathway); NO_x validation against field data remains an open item, discussed in Section 3.7.

3.3. The effect of natural gas composition on temperature distribution

This section analyzes the thermodynamic response of the boiler combustion chamber to different natural gas compositions under a constant heat input of 11,704 kW and an excess air ratio of 16%. Maintaining a constant heat input is essential because it isolates the effect of fuel composition from the effect of boiler load. Therefore, the observed temperature differences can be attributed mainly to changes in fuel molecular structure, stoichiometric oxygen demand, dilution effect, and spatial heat-release distribution rather than to differences in supplied thermal power.

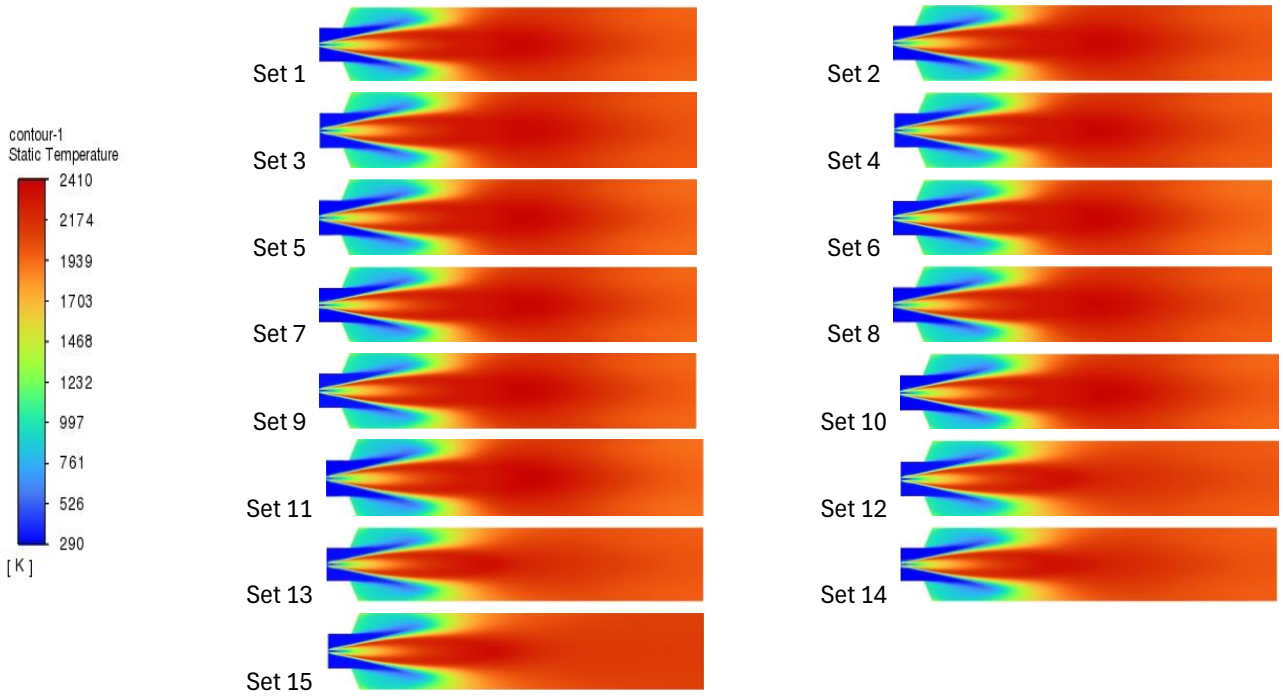

Figure 5. Temperature distribution (K) contours in the combustion chamber for the fifteen fuel-composition sets defined in Table 4, obtained at the constant heat input of 11,704 kW and 16% excess air.

The temperature contours in Figure 5 show that all cases develop high-temperature zones near the main combustion region, followed by redistribution of thermal energy along the furnace length. However, the intensity and spatial uniformity of these zones differ among fuel compositions. Average combustion chamber temperatures range from 1825.04 K in Set 13 to 1864.08 K in Set 7, while maximum temperatures range from 2324.91 K in Set 14 to 2401.75 K in Set 11. This indicates that fuel composition affects not only the global furnace temperature but also the formation of localized hot spots, which are critical for thermal stress and NO_x formation.

A comparison among Sets 12, 13, and 14 is particularly important because these cases represent field-realistic multicomponent natural gas compositions with different proportions of heavier hydrocarbons and inert species.

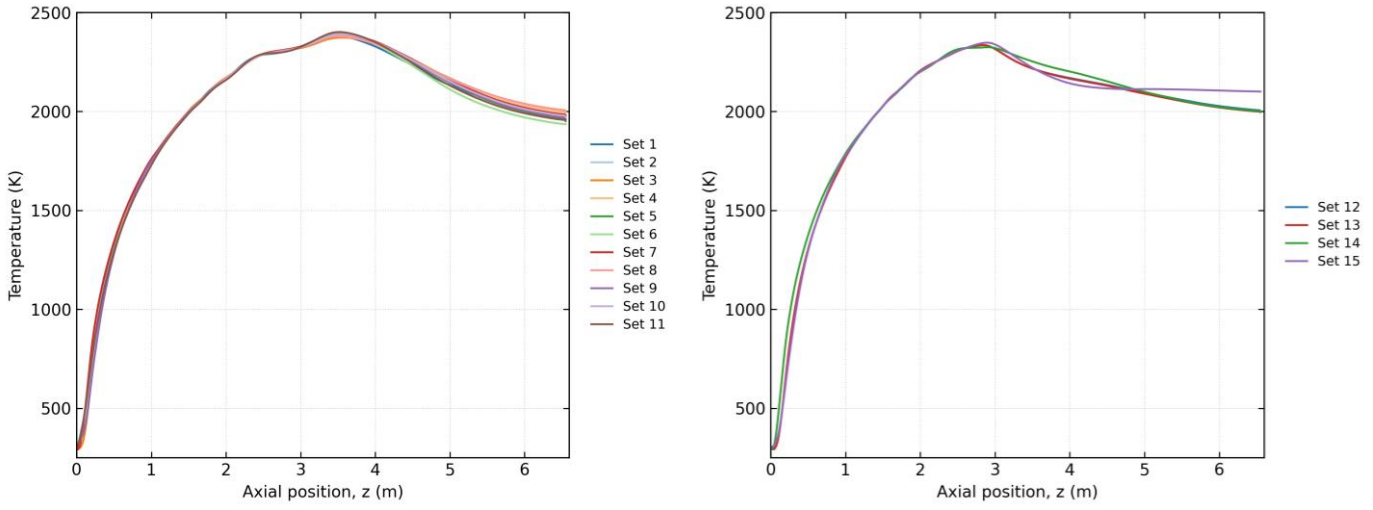

Figure 6. Temperature (K) versus axial position (z) along the combustion-chamber centerline for fuel-composition Sets 1–15: (a) simplified laboratory-style Sets 1–11; (b) field-realistic, GC-verified Sets 12–15. The peak of each curve corresponds to the maximum temperature reported for that set in Table 6.

Set 12 produces an average temperature of 1826.02 K, Set 13 produces 1825.04 K, and Set 14 produces 1855.59 K. The higher average temperature in Set 14 suggests that changes in the relative fraction of C2+ hydrocarbons can alter the spatial heat-release pattern even when the overall heat input remains constant. This result is consistent with the combustion principle that heavier alkanes generally have different oxidation pathways, molecular weights, and local heat-release characteristics compared with methane-dominant mixtures.

The maximum temperature data in Figure 6 provides a more engineering-relevant interpretation than average temperature alone. Set 11 generates the highest maximum temperature of 2401.75 K, suggesting stronger localized heat release and a higher probability of hot-spot formation. In contrast, Sets 12–15 exhibit lower maximum temperatures, ranging from 2324.91 K to 2347.92 K, indicating a more uniform thermal field. This finding is important for boiler operation because localized high-temperature regions can accelerate tube degradation, increase thermal fatigue, and intensify thermal NO_x formation. Therefore, temperature uniformity should be considered together with average furnace temperature when evaluating the suitability of a fuel composition for industrial boiler combustion.

Set 15, which contains nitrogen as an inert component, demonstrates the role of dilution in controlling the thermal field. Although nitrogen lowers the effective heating value of the fuel mixture, the constant heat input condition requires a compensating adjustment in fuel flow rate. As a result, the average furnace temperature remains comparable to other cases, but the maximum temperature is suppressed. This behavior shows that inert gas dilution does not simply reduce the bulk combustion temperature; rather, it redistributes thermal energy and reduces the severity of localized hot spots. Such a mechanism agrees with previous findings that inert species such as N_2 and CO_2 can act as heat sinks and suppress peak flame temperature due to their thermal capacity. These findings align with research by Lee et al. (2013), which states that inert components like N_2 and CO_2 in gas fuels have higher specific heat capacities than hydrocarbons, thus serving as local heat sinks that smooth temperature profiles. In boiler operations, this more uniform temperature distribution is generally preferred as it reduces thermal fatigue risk on boiler wall materials [23].

3.4. The effect of natural gas composition on CO_2

The CO_2 distribution results in Figure 7 and Figure 8 show that carbon dioxide formation follows a similar spatial pattern for all fuel compositions. CO_2 concentration increases rapidly in the initial combustion zone, reaches a maximum in the main reaction region, and gradually stabilizes toward the downstream section of the furnace.

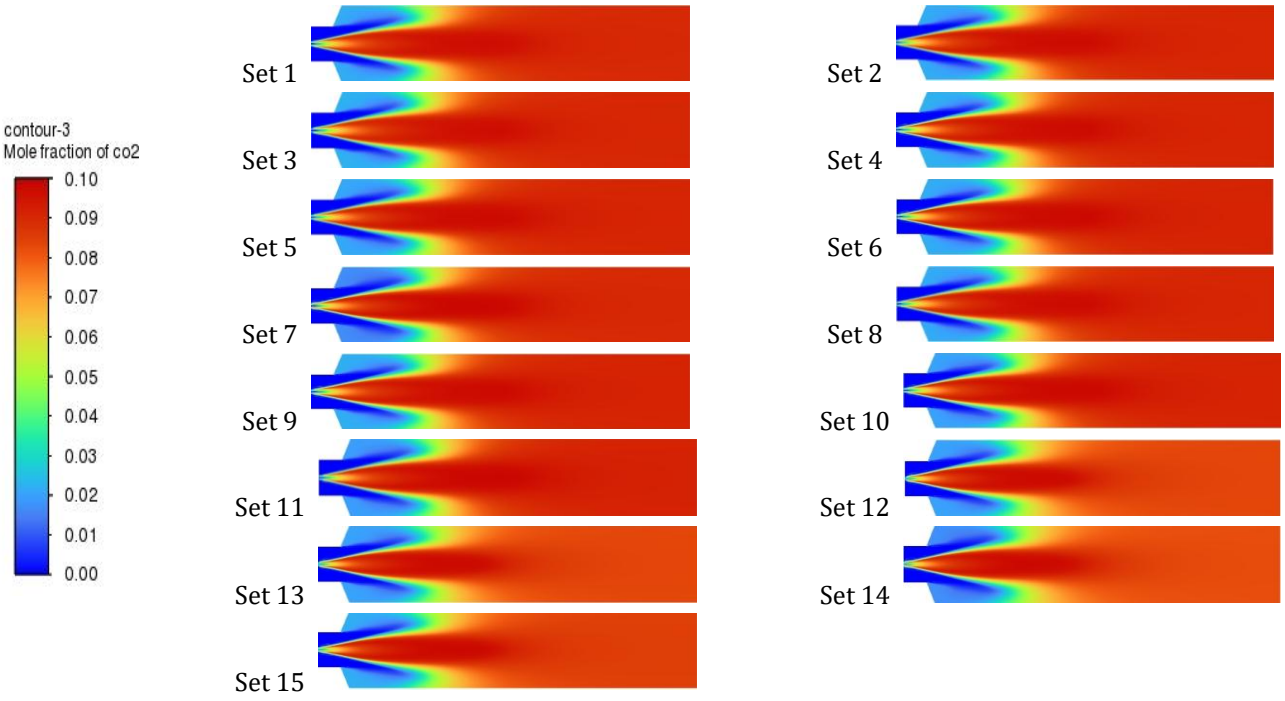

Figure 7. CO_2 mole-fraction distribution contours in the combustion chamber for fuel-composition Sets 1–15 (Table 4).

This trend confirms that the dominant carbon oxidation pathway remains similar across all cases because the fuels are hydrocarbon-based and the simulations are conducted under the same excess air ratio.

Average CO_2 mole fractions in exhaust gases across all variations show a relatively narrow range, from 7.963% (Set 3) to 8.296% (Set 15). Although the absolute range appears small, the proportional difference reaches approximately 4.2%. Compared with temperature and NO_x, CO_2 is therefore less sensitive to fuel composition under constant heat input. This relatively narrow range occurs because the boiler thermal load is fixed, so the total amount of fuel energy supplied to the furnace remains constant even though the fuel composition changes. However, the small numerical variation is still relevant at industrial scale because continuous boiler operation can convert minor concentration changes into significant cumulative emissions over long operating periods.

Interestingly (Figure 7), Set 15 with 2.3% N_2 produces the highest CO_2 concentration despite having the lowest heating value. This result can be explained by the constant heat input constraint: when the heating value decreases due to inert dilution, a slightly higher fuel flow rate is required to maintain the same thermal duty. The increased fuel flow increases the amount of carbon introduced into the combustion chamber per unit time, thereby increasing the CO_2 concentration in the flue gas. This shows that CO_2 emissions should not be interpreted only from the mole fraction of carbon-bearing species in the fuel; they must also be evaluated together with LHV, fuel mass flow rate, and operating load.

The similarity of CO_2 levels in Sets 12–14 also suggests that different C2+ alkane distributions do not strongly alter total CO_2 concentration when the total carbon input and heat duty are comparable. Therefore, from an emission-control perspective, fuel composition management has a stronger influence on NO_x than on CO_2 concentration in the present boiler configuration. This distinction is important because CO_2 is mainly governed by carbon balance and heat input, whereas NO_x is highly affected by local temperature, residence time, oxygen availability, and reaction-zone structure.

The engineering implication is that CO_2 monitoring alone is insufficient to evaluate the combustion impact of natural gas composition. A fuel composition that produces similar CO_2 concentration may still generate substantially different NO_x levels due to different local flame temperatures and hot-spot distributions. This aligns with combustion stoichiometry: while ethane, propane, and butane produce different moles of CO_2 per mole of fuel, their carbon intensity per unit mass energy remains comparable [24]. Figure 8 illustrates the mole fraction distribution of carbon dioxide (CO_2) versus flow position along the combustion chamber for various operating conditions represented by Sets 1 through 15. Generally, all curves exhibit similar trend characteristics: rapid CO_2 concentration increase in the initial combustion zone, reaching maximum levels in the core flame region, followed by gradual decline toward stable conditions at the end of the combustion domain.

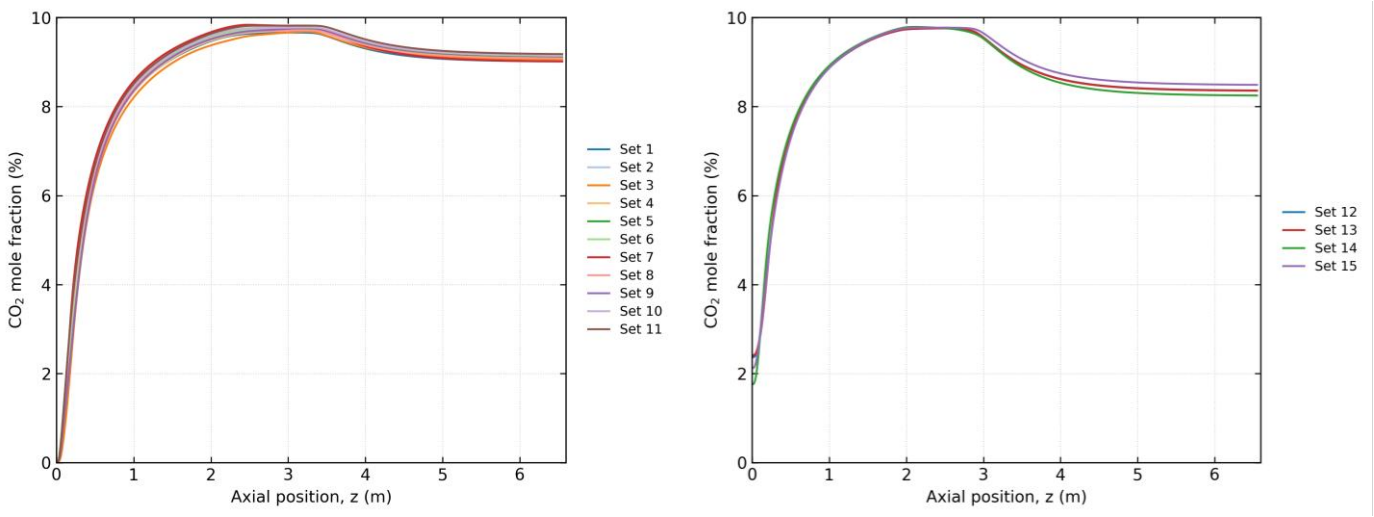

Figure 8. CO_2 mole fraction (%) versus axial position (z) along the combustion-chamber centerline for fuel-composition Sets 1–15: (a) simplified laboratory-style Sets 1–11; (b) field-realistic, GC-verified Sets 12–15.

This pattern indicates that CO_2 formation mechanisms across variations are primarily governed by similar hydrocarbon oxidation phenomena, despite minor differences due to operational parameter variations. In the initial combustion region (x = 0–1 m), CO_2 concentration rises sharply from near-zero values to 0.08–0.09. This reflects highly intensive fuel oxidation immediately after fuel-oxidizer mixing. During this early stage, combustion temperatures surge due to exothermic reaction energy release, dramatically accelerating chemical reaction rates. Fuel-bound carbon reacts with oxygen to form carbon monoxide (CO) as an intermediate product, which is then further oxidized to carbon dioxide (CO_2). Subsequently, in the mid-combustion chamber region (x = 1.5–3.5 m), CO_2 mass fraction peaks between 0.095–0.098. This zone is identifiable as the main combustion zone, where carbon oxidation reactions proceed most optimally. The high CO_2 concentration here signifies successful conversion of most fuel carbon content to complete combustion products. At this phase, furnace temperatures are elevated and relatively stable, placing oxidation reaction kinetics at peak conditions.

3.5. The effect of natural gas composition on NO_x

As established in Section 2.3, NO_x formation in this study is governed by the thermal (extended Zeldovich) mechanism, in which molecular nitrogen is oxidized via Equations (22)–(23) in high-temperature, oxygen-rich regions near and downstream of the flame front. This mechanism is highly sensitive to local temperature, oxygen availability, and residence time, and is markedly accelerated above approximately 1,800 K.

The contour result in Figure 9 indicates that NO_x formation is concentrated in high-temperature flame regions and then transported downstream with the combustion products. This spatial behavior is consistent with the thermal NO_x mechanism, where nitrogen oxidation is accelerated at elevated temperature and sufficient oxygen availability. However, the comparison among cases shows that high LHV or heavier alkane content does not automatically produce the highest NO_x. Instead, NO_x formation depends strongly on how the fuel composition modifies the local flame structure, radical formation, residence time, and temperature uniformity within the boiler chamber.

NO_x emissions represent the parameter most sensitive to fuel composition changes among all analyzed variables. Average NO_x concentrations range from a minimum of 25.88 ppm (Set 14) to a maximum of 51.05 ppm (Set 9). This case contains a multicomponent C_2–C_5 alkane mixture that appears to promote localized high-temperature reaction zones.

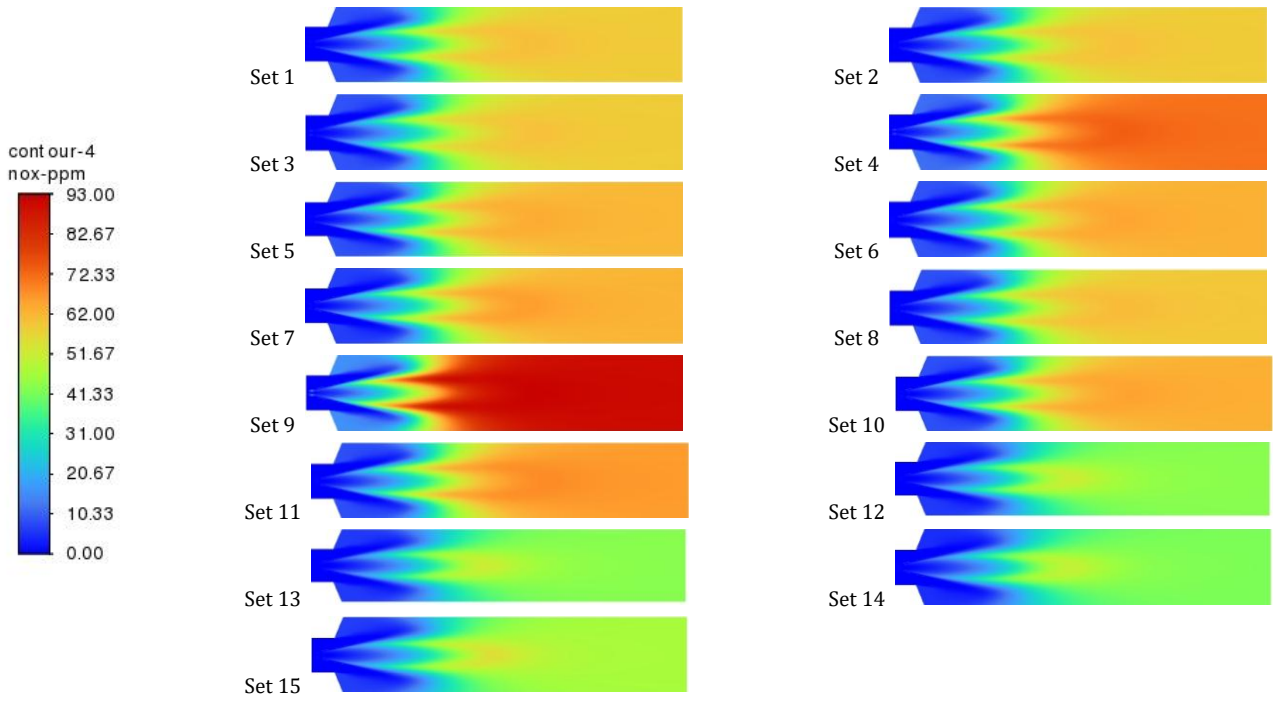

Figure 9. Thermal NO_x concentration contours in the combustion chamber for fuel-composition Sets 1–15 (Table 4).

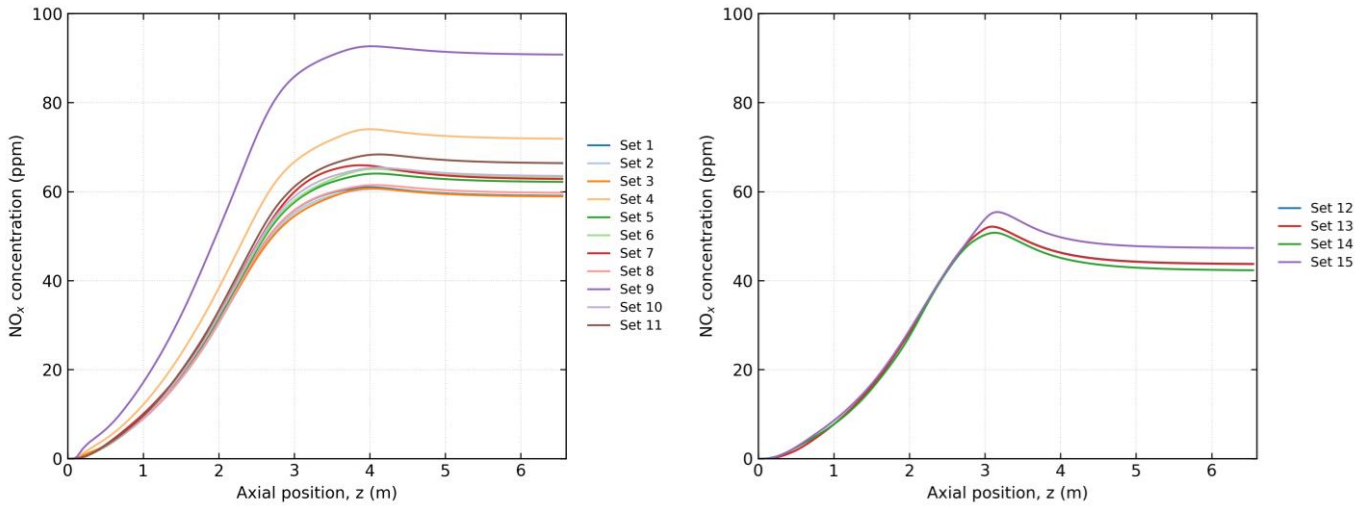

Figure 10. Thermal NO_x concentration (ppm) versus axial position (z) along the combustion-chamber centerline for fuel-composition Sets 1–15: (a) simplified laboratory-style Sets 1–11; (b) field-realistic, GC-verified Sets 12–15. The peak of each curve corresponds to the maximum NO_x concentration reported for that set in Table 6.

Although its average temperature is not the highest among all cases, its NO_x level is the highest, indicating that local hot spots and reaction-zone distribution are more decisive for NO_x formation than domain-averaged temperature alone. This finding is important because many simplified combustion assessments use average temperature or LHV as a proxy for NO_x tendency, which may lead to inaccurate interpretation in practical boiler geometries.

Conversely, Set 14 (88% CH_4 + 12% C_2–C_5 N_2+CO_2 blend) yields the lowest average NO_x at 25.88 ppm, half of Set 9's value, with a maximum of only 50.76 ppm. This counterintuitive result, where heavy alkanes do not consistently produce more NO_x, indicates that the composition- NO_x relationship depends heavily on spatial reaction distribution within specific boiler geometries, beyond just fuel thermodynamic properties.

Field-realistic compositions represented by Sets 12–15 consistently generate lower average NO_x values of 25.88–28.01 ppm, compared with 31.93–51.05 ppm for the academically designed compositions represented by Sets 1–11. This corresponds to an approximate 30–49% reduction in NO_x for field-realistic compositions. The lower NO_x level is associated with more distributed reaction zones, the presence of inert species, and reduced peak temperature intensity. This result provides a practical engineering implication: industrial users may reduce NO_x emissions by controlling or selecting natural gas composition before implementing hardware-based solutions such as burner replacement, staged combustion, flue gas recirculation, or post-combustion treatment.

The NO_x trend along the furnace length, shown in Figure 10, increases rapidly in the early combustion zone and then approaches a plateau downstream. This indicates that NO_x is mainly formed during the initial high-temperature reaction period, while downstream regions primarily transport or slightly redistribute the formed NO_x. Therefore, emission mitigation strategies should focus on controlling peak temperature and oxygen availability near the flame front rather than only treating the exhaust gas after the main combustion process is complete. Results align with Patel [25], emphasizing spatial energy distribution's role in NO_x emission control. In Figure 10, the NO_x graph demonstrates that NO_x concentrations rise sharply with path length up to approximately 3–4 m, then plateau or slightly decline downstream. Scientifically, this pattern results from dominant NO_x formation processes in the initial zone, followed by the system approaching thermal and chemical equilibrium along the flow path. In the early path section, NO_x buildup occurs due to high gas temperatures, oxygen availability, and sufficient residence time facilitating NO_x formation primarily via thermal-NO_x mechanisms highly sensitive to temperature. From a chemical engineering perspective, NO_x formation generally accelerates when atmospheric nitrogen oxidation reactions proceed at elevated temperatures, with formation rates tracking temperature increases and reactant mixing intensity.

3.6. The effect of temperature on NO_x formation

The relationship between maximum adiabatic flame temperature and peak nitrogen oxide (NO_x) concentration across Set 1 through Set 15 is presented in Figure 11, demonstrating a consistent positive correlation between these two parameters throughout the entire range of fuel composition variations. The fuel blends employed in this study were systematically formulated by varying the molar fractions of hydrocarbon components including methane (CH_4), ethane (C_2H_6), propane (C_3H_8), butane (C_4H_{10}), pentane (C_5H_{12}), and hexane (C_6H_{14}) while maintaining a constant stoichiometric air-to-fuel ratio (AFR) in the range of 16.81–17.09 kg air/kg fuel across all sets, as detailed in Table 4 and Table 5.

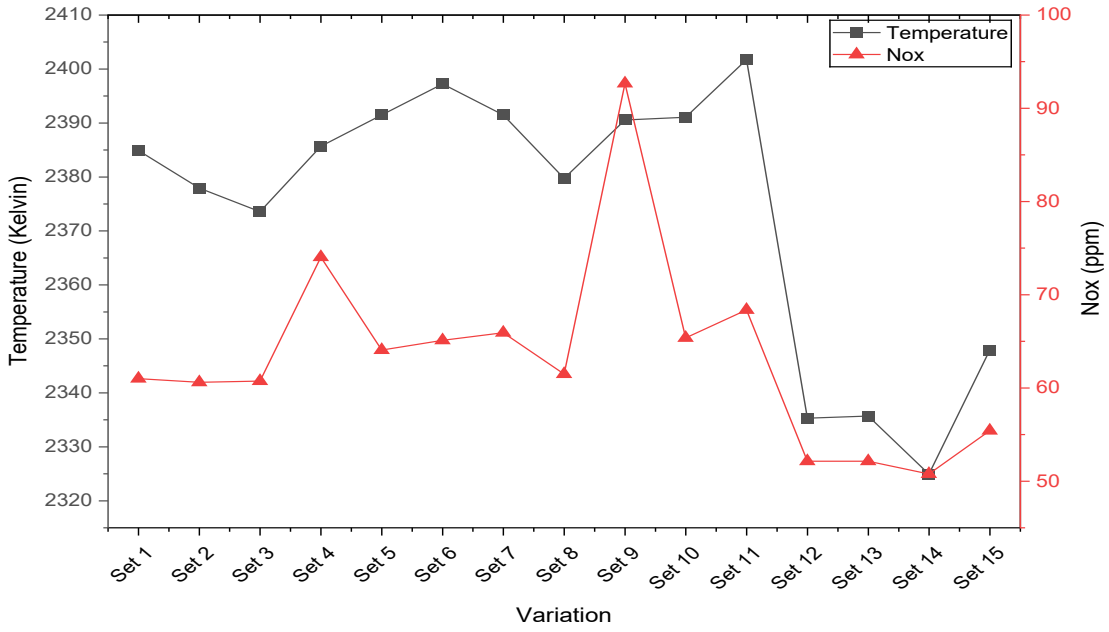

Figure 11. Correlation between the maximum adiabatic flame temperature (K) and the peak NO_x concentration (ppm) for fuel-composition Sets 1–15 (Table 6), showing a consistent positive relationship across the full range of compositions studied.

For Sets 1 through 11, the fuel was predominantly composed of methane (CH_4, molar fraction = 0.88), supplemented by varying proportions of ethane (0.054–0.096), propane (0.018–0.048), and butane (0.0084–0.024), with no addition of higher hydrocarbons or inert diluents. This group produced relatively high lower heating values (LHV) for the fuel mixture, ranging from 49.07 to 49.36 MJ/kg, and correspondingly elevated maximum flame temperatures between 2373.55 K and 2401.75 K. These thermodynamic conditions directly drove elevated peak NO_x concentrations, spanning from 60.60 ppm to 92.66 ppm. The strong dependence of NO_x formation on flame temperature observed in this group is consistent with the extended Zeldovich thermal NOx mechanism, in which the dissociation of molecular nitrogen (N_2) and its subsequent oxidation to nitric oxide (NO) are highly temperature-sensitive reactions that accelerate exponentially above approximately 1,800 K [26].

As established by Bani et al. (2024), the adiabatic flame temperature of natural gas mixtures containing methane, ethane, and propane is primarily governed by the mixture's heating value and the molar composition of the hydrocarbon blend, with heavier alkanes contributing marginally to higher flame temperatures through their greater carbon-to-hydrogen ratios [27]. Accordingly, the variation in NO_x concentrations across Sets 1–11 can be attributed to the subtle differences in LHV arising from the substitution of lighter alkanes (ethane, propane) with slightly heavier components (butane), which marginally modified the energy content and peak temperature of the flame, thereby modulating the rate of thermal NO_x formation. This observation aligns with the findings of Dong et al. (2023), who reported that combustion characteristics including peak temperature and NO_x yield are strongly sensitive to fuel composition, even for relatively minor changes in alkane chain length within a methane-dominant mixture [28].

The highest flame temperature (2401.75 K) and the NO_x concentration (68.36 ppm) were recorded at Set 11, while Set 9 exhibited the highest average NO_x of 92.66 ppm at a

maximum temperature of 2390.56 K. These peak values are consistent with the thermodynamic threshold behavior described by Marzouk (2023), in which flame temperatures exceeding 2200 K under stoichiometric air-methane combustion conditions are sufficient to sustain rapid O and OH radical generation, accelerating the first and second Zeldovich reactions and culminating in substantially elevated NO formation rates [29].

In contrast, a pronounced simultaneous reduction in both maximum flame temperature and peak NO_x emissions was observed for Sets 12 through 15. In this group, the molar fraction of ethane was drastically reduced to 0.031–0.037, while significant additions of pentane (C_5H_{12} = 0.0025), hexane (C_6H_{14} = 0.0228–0.0292), and molecular nitrogen (N_2 = 0.0176–0.0241) were introduced into the fuel mixture. Despite the slight increase in LHV observed for these sets (49.30–49.32 MJ/kg), due to the higher energy density of C_5–C_6 alkanes, the maximum flame temperatures declined markedly to the range of 2324.91–2347.92 K, accompanied by a reduction in peak NO_x concentrations to 50.77–55.40 ppm representing an overall decrease of approximately 35–45% relative to the peak values recorded for Sets 1–11.

This apparent contradiction between elevated LHV and reduced flame temperature can be explained by the thermophysical role of molecular nitrogen as an inert diluent within the fuel stream. The nitrogen component acts as a heat sink, absorbing sensible heat from the combustion products without participating in exothermic reactions, thereby lowering the effective adiabatic flame temperature of the mixture [30]. This mechanism is well established in combustion literature: the introduction of inert diluents such as N_2 or CO_2 into the fuel mixture reduces the volumetric heat release rate per unit mass of the combustion products and consequently suppresses the thermal NO_x formation pathway by maintaining flame temperatures below the critical exponential reaction threshold of the Zeldovich mechanism [28]. Furthermore, the mass flow rates of both fuel and air were slightly higher in Sets 12–15 (air flow rate = 4.702–4.703 kg/s) compared to Sets 1–11 (4.646–4.650 kg/s), indicating that the dilution-induced suppression of flame temperature and NO_x was sufficiently dominant to overcome the marginal increase in absolute heat input.

Taken together, the results presented across all 15 fuel composition sets clearly demonstrate that the adiabatic flame temperature is the primary thermodynamic driver of NO_x formation under stoichiometric combustion conditions, and that fuel composition particularly the proportion of inert nitrogen diluent serves as a critical control variable for emission mitigation. The nitrogen dilution strategy adopted in Sets 12–15 proved effective in reducing peak NO_x emissions by approximately 35–45% compared to the methane-dominant sets, without altering the air-to-fuel stoichiometry, underscoring its practical relevance as a low-NO_x combustion strategy for gas-phase fuel systems with variable composition.

To place these results in the context of previous work, Table 9 summarizes how the present findings agree or diverge with prior studies on fuel-composition and dilution effects on combustion temperature and NO_x formation, together with the corresponding scientific explanation for each comparison.

Table 9. Comparison of key findings from the present study with previous literature on the effects of fuel composition and inert-gas dilution on combustion temperature and NO_x formation, indicating agreement (A), partial discrepancy (PD), or an addressed research gap (G) for each aspect.

Aspect	Previous study	Present study	Agreement / discrepancy and explanation
Multicomponent fuel blends and NOx	Zhu et al. [7]: multicomponent mixtures can lower NOx via improved heat distribution and reduced hot spots (coal-fired boiler)	Field-realistic Sets 12–15 show 30–49% lower NOx than simplified Sets 1–11	(A) Agreement. Distributed reaction zones and inert dilution reduce localized peak temperature, consistent with the heat-distribution mechanism proposed by Zhu et al.
NOx vs. heating value as a proxy	Min et al. [8]: NOx cannot be explained by heating value alone; depends on spatial combustion characteristics	Set 14 (C1–C5 N2+CO2 blend) shows the lowest NOx despite comparable LHV to Set 9 (highest NOx) (Novel Finding 1)	(A) Agreement. Confirms a geometry- and distribution-dependent NOx mechanism rather than an LHV-based proxy.
Drivers of CO2 emission	Wright et al. [6]: CO2 is tied to oxidized carbon, modulated by excess air and dilution	Set 15 shows the highest CO2 among Sets 12–15 despite the lowest LHV, due to the higher fuel flow rate required	(A) Agreement. Confirms CO2 is governed by carbon throughput and dilution/flow-rate effects rather than composition alone.

Aspect	Previous study	Present study	Agreement / discrepancy and explanation
Heavier alkanes and flame temperature	Bani-Hani et al. [27]: heavier alkanes marginally raise adiabatic flame temperature via a higher carbon-to-hydrogen ratio	Sets 1–11 (non-diluted) reaches a higher maximum temperature (up to 2401.75 K) than Sets 12–15 (2324.91–2347.92 K) despite the latter having slightly higher LHV	(PD) Partial discrepancy. The trend holds within Sets 1–11 alone, but is overridden in Sets 12–15 by the dominant heat-sink effect of inert N2; composition effects are secondary to dilution when both are present.
Inert-gas dilution and NOx suppression	Yilmaz et al. [30] and Dong et al. [28]: N2/CO2 dilution lowers flame temperature and suppresses the thermal- NOx pathway	Set 12-15 (2.3 % N2) shows suppressed maximum temperature and among the lowest NOx (55.41 ppm) despite its lower LHV	(A) Agreement. Confirms N2 acts as a heat sink; extends this mechanism to a constant-heat-input industrial boiler condition.
Heat-sink role of inert species	Lee et al. [23]: inert components (N2, CO2) have higher specific heat capacity, smoothing temperature profiles	Set 15 shows an average temperature comparable to non-diluted cases but a suppressed maximum temperature, i.e., redistributed rather than simply reduced	(A) Agreement, with refinement. Extends Lee et al.'s finding by showing a redistribution mechanism specific to fixed heat-input operation.
Threshold temperature for rapid thermal- NOx formation	Marzouk [29]: flame temperature above = 2200 K sustains rapid O/OH radical generation, accelerating the Zeldovich reactions	Sets 9 and 11 (highest NOx) reach 2390.56–2401.75 K, consistent with this threshold; Sets 12–15 (2324.91–2347.92 K) still exceed 2200 K but show markedly lower NOx	(PD) Partial agreement. Confirms the general threshold, but shows that above ≈ 2200 K, NOx is further modulated by local residence time and reaction-zone distribution, not temperature alone.
Scope: industrial-scale vs. laboratory/domestic validation	Erne et al. [9]: surface-stabilized combustion studied in a laboratory-scale, domestic condensing boiler	This study models a medium-capacity (17 t/h) industrial boiler, validated against field commissioning measurements	(G) Addresses a gap. Provides field-relevant validation lacking in prior lab-scale studies, supporting the applicability of the present findings to industrial operation.
Composition-driven NOx trend: hydrogen doping vs. heavier-alkane substitution	Wang et al. [31] (2025): CFD study of a 2.1 MW industrial boiler shows that increasing the hydrogen fraction in hydrogen-doped natural gas (0–25%) raises flame temperature and NOx emissions monotonically, via hydrogen's higher adiabatic flame temperature and laminar flame speed	Substituting heavier alkanes for methane (Sets 1–11) does not raise NOx monotonically: Set 14 (C_1–C_5 N_2+CO_2 blend) yields the lowest NOx among all fifteen sets studied (Novel Finding 1)	(PD) Partial discrepancy, fuel-axis dependent. Both studies confirm the same underlying temperature–thermal- NOx mechanism, but show it manifests differently across composition axes: H2 blending alters flame chemistry and laminar flame speed directly, producing a monotonic trend, whereas heavier-alkane substitution within a methane-dominant blend interacts with spatial reaction-zone distribution in a way that a single-variable (LHV or additive-fraction) proxy cannot capture.
NOx mitigation pathway: burner-hardware redesign vs. fuel-composition management	Mubashir et al. [32] (2025): machine-learning-assisted CFD optimization of burner geometry (folded flame pattern, fuel staging) achieved a 31% NOx reduction by lowering and redistributing peak flame temperature, independent of fuel composition	Field-realistic multicomponent compositions with N2 dilution (Sets 12–15) achieve a comparable 30–49% NOx reduction through fuel composition management alone, with no burner or hardware modification	(A) Agreement, complementary mechanism. Both studies converge on peak-temperature redistribution as the operative NOx suppression mechanism; the present results indicate that composition management and hardware redesign act on the same physical pathway and could, in principle, be combined for greater cumulative NOx reduction in industrial gas-fired equipment.

The present findings agree closely with the established roles of multicomponent blending, inert-gas dilution, and NO_x mitigation mechanisms reported in prior literature (rows 1, 2, 3, 5, 6, and 10 of Table 9), while also revealing partial discrepancies with single-mechanism

or single-composition-axis literature (rows 4, 7, and 9) that are resolved once the combined, rather than isolated, effect of heavier-alkane content and nitrogen dilution is considered. In addition, the present study addresses a validation-scope gap left open by prior laboratory and domestic scale investigations by validating the model against industrial-scale commissioning data (row 8). This distinction is the central contribution of the present study relative to prior work, and it is only observable because the fifteen sets examined here vary composition and dilution jointly under a realistic, field-validated industrial boiler geometry rather than in isolation.

3.7. Model limitations and novel findings

Three modeling simplifications should be considered when interpreting the absolute magnitudes reported in this study: (i) the adiabatic furnace-wall assumption (Section 2.4), which neglects real water-tube heat extraction and is expected to overpredict peak temperature and thermal NO_x; (ii) the Eddy Dissipation Model with one-step global chemistry (Section 2.3), which does not resolve finite-rate kinetics; and (iii) grid independence (Section 2.6), which was assessed using domain-averaged outlet temperature rather than a NO_x -specific local metric. All three were applied uniformly across the fifteen fuel-composition cases, so their effect on the relative comparisons between compositions, the primary object of this study is expected to be considerably smaller than their effect on absolute values. This is supported by the validation in Section 3.2, where the combustion stoichiometry framework reproduces measured dry-basis CO_2 within 0.27–2.00% across the full load range (mean deviation 1.17%), despite these simplifications, since CO_2 is governed mainly by carbon balance rather than the temperature-sensitive NO_x pathway. NO_x itself could not be field-validated, as the available commissioning data does not include a NO_x measurement. Priority directions for future refinement include a non-adiabatic or conjugate wall boundary condition informed by the boiler's actual water-side heat transfer, a finite-rate closure such as the Eddy Dissipation Concept (EDC) with reduced or detailed kinetics, a dedicated NO_x -specific grid-convergence study, and field validation against a directly measured NO_x concentration from the same boiler unit.

Notwithstanding these limitations, the simulation results presented in this study contribute three specific findings that are limited in previously reported literature on natural gas combustion in industrial diffusion-flame boilers. Novel Finding 1 Non-monotonic NO_x response to alkane chain length under identical thermal load conditions**.** It is generally expected from thermodynamic considerations that heavier alkanes, having higher LHV, would produce elevated flame temperatures and consequently higher NO_x concentrations. This study demonstrates that this relationship does not hold monotonically in a real boiler geometry: Set 14 (88% CH_4 + 12% C_2–C_5 N_2+CO_2 blend), produces the lowest average NO_x among all field-realistic cases (25.88 ppm), while Set 9 (CH_4 + C_2H_6 + C_3H_8 + C_4H_{10} + C_5H_{12} mixture) produces the highest average NO_x (51.05 ppm) despite a comparable LHV. This finding, which reveals a geometry- and distribution-dependent NO_x mechanism, challenges the simplification commonly applied in combustion engineering practice of using LHV as a proxy for NO_x tendency in multi-component fuels.

Novel Finding 2 Systematic quantification of the emission gap between field-realistic and laboratory-simplified compositions**.** This study provides the first quantitative comparison, to the authors' knowledge, between NO_x emissions from academically simplified compositions (simplified laboratory-style blends dominant, Sets 1–11) and field-realistic multi-component compositions (Sets 12–15) in an industrial boiler at constant thermal load. The results demonstrate a consistent 30–49% NO_x reduction in field-realistic compositions (25.88–28.01 ppm) versus simplified compositions (31.93–51.05 ppm).

Novel Finding 3 Nitrogen diluent as a decoupled temperature-moderating mechanism at constant heat input In fixed heat-input boiler operation, where fuel flow rate adjusts to compensate for changes in LHV, the field-realistic compositions (Sets 12–15) carry an inherent inert background (2.3 mol% N_2 plus 1.76–2.41 mol% CO_2) absent from Sets 1–11. Set 15, the representative case within this group, illustrates the resulting thermal profile most clearly: average furnace temperature (1832.66 K) remains within the range of the non-diluted cases despite a substantially lower fuel LHV, yet maximum temperature (2347.92 K) and peak NO_x (55.41 ppm) are among the lowest observed across all fifteen sets. This demonstrates that inert dilution functions as a spatial heat redistributor rather than a bulk heat reducer under constant-load boiler conditions a mechanism not previously described for this capacity class, and one that carries implications for the use of high-nitrogen natural gas in emission-sensitive applications.

4. Conclusions

Based on the simulation results and analysis of fifteen natural gas composition variations in a 17 ton/hour capacity boiler with constant heat input of 11,704 kW, the following conclusions can be drawn. This study demonstrates that natural gas composition is not only a fuel-quality parameter but also a significant operational variable affecting combustion temperature distribution and NO_x formation in industrial steam boilers. Natural gas fuel composition significantly influences combustion chamber temperature distribution, with average temperatures ranging from 1825 K to 1864 K and maximum temperatures from 2324 K to 2401 K. More complex heavy alkane compositions (C_2–C_5 mixtures) tend to produce higher average temperatures, while nitrogen addition as a diluent effectively promotes uniform temperature distribution. This finding indicates that small variations in fuel composition can alter thermal behavior inside the furnace even when the boiler operates under the same heat input and excess air ratio. Exhaust CO_2 concentrations exhibit relatively low sensitivity to fuel composition variations under constant heat input, with total variation around 4.2%. However, nitrogen addition lowers the heating value yet increases CO_2 concentration due to the higher required fuel flow rate to maintain thermal power. Therefore, CO_2 concentration alone is not sufficient to evaluate the combustion impact of natural gas composition because it is affected by the combined effects of carbon content, fuel flow rate, heating value, and dilution. Thermal NO_x emissions are the most responsive parameter to composition changes, ranging from 25.88 to 51.05 ppm. Field-realistic compositions, represented by Sets 12–15, consistently yield lower NO_x averages of 25.88–28.01 ppm compared to academically designed variations, represented by Sets 1–11, which produce 31.93–51.05 ppm. The 97.3% difference between the lowest and highest NO_x values confirms that fuel composition alone can cause nearly twofold variation in NO_x emission under identical boiler operating conditions. This provides a clear engineering implication that fuel composition screening can be used as a low-intervention NO_x mitigation strategy before applying more capital-intensive technologies such as burner modification, flue gas recirculation, or post-combustion treatment. This study contributes to the existing body of knowledge by systematically evaluating realistic multi-component natural gas compositions in a medium capacity industrial boiler under constant heat input conditions. In contrast to previous studies that commonly simplify natural gas as a methane-dominated fuel or focus primarily on emission control hardware, the present work demonstrates that heavier alkane fractions and inert gas dilution can directly influence furnace temperature uniformity and NO_x distribution. These findings provide new insight into the role of fuel composition management in supporting combustion optimization, emission control, and fuel procurement decisions for industrial boiler operation. For future work, experimental validation using field boiler emission data and flue gas measurements should be conducted to strengthen the numerical findings. The integration of CFD results with real-time fuel gas composition monitoring is also recommended to develop practical combustion tuning strategies for industrial boiler systems.

Acknowledgement

The authors would like to thank the Department of Mechanical Engineering, State University of Surabaya, for providing the laboratory facilities and computational resources used to carry out this study. The authors also gratefully acknowledge the industrial partner who granted access to the boiler commissioning records and gas-chromatography fuel composition data used for model validation.

Declaration of Generative AI and AI-Assisted Technologies in the Writing Process

The authors used Claude AI (Anthropic) to assist in refining and clarifying the written presentation of the manuscript, including improving the clarity of descriptions and introductory explanations initially drafted by the authors. All AI-generated content was critically reviewed, revised, and validated by the authors. The authors take full responsibility for the scientific accuracy, originality, and integrity of the manuscript, in accordance with the guidelines of the Committee on Publication Ethics (COPE). The primary data and numerical simulations were conducted independently by the authors using Computational Fluid Dynamics (CFD) methodology in ANSYS Fluent. AI assistance was strictly limited to language refinement and did not contribute to data collection, simulation processes, analysis, or scientific interpretation.

References

[1] International Energy Agency, *World Energy Outlook 2023*. Paris, France: IEA, 2023. [Online]. Available: https://www.iea.org/reports/world-energy-outlook-2023. Accessed: Aug. 10, 2026.

[2] H. D. R. Nuryanto, "CO_2 capture using dissolved ammonia (NH_4OH)—Article review," *Rekayasa Mesin*, vol. 16, no. 3, pp. 1155–1168, 2025, doi: 10.21776/jrm.v16i3.2135.
[3] T. Wang, H. Zhang, Y. Zhang, H. Wang, J. Lyu, and G. Yue, "Efficiency and emissions of gas-fired industrial boiler fueled with hydrogen-enriched natural gas: A case study of 108 t/h steam boiler," *Int. J. Hydrogen Energy*, vol. 47, no. 65, pp. 28188–28203, Jul. 2022, doi: 10.1016/j.ijhydene.2022.06.121.
[4] M. S. Cellek and A. Pınarbaşı, "Investigations on performance and emission characteristics of an industrial low swirl burner while burning natural gas, methane, hydrogen-enriched natural gas and hydrogen as fuels," *Int. J. Hydrogen Energy*, vol. 43, no. 2, pp. 1194–1207, Jan. 2018, doi: 10.1016/j.ijhydene.2017.05.107.
[5] A. Franco and M. Rocca, "Industrial decarbonization through blended combustion of natural gas and hydrogen," *Hydrogen*, vol. 5, no. 3, pp. 519–539, Aug. 2024, doi: 10.3390/hydrogen5030029.
[6] M. L. Wright and A. C. Lewis, "Emissions of NOx from blending of hydrogen and natural gas in space heating boilers," *Elementa Sci. Anthropocene*, vol. 10, no. 1, Art. no. 00114, May 2022, doi: 10.1525/elementa.2021.00114.
[7] B. Zhu, B. Shang, X. Guo, C. Wu, X. Chen, and L. Zhao, "Study on combustion characteristics and NOx formation in 600 MW coal-fired boiler based on numerical simulation," *Energies*, vol. 16, no. 1, Art. no. 262, Dec. 2023, doi: 10.3390/en16010262.
[8] C. Min, S. Xu, Y. Yang, and P. Wang, "Effect of different flue gas recirculation rates on low-NOx combustion characteristics: A numerical simulation based on the combustion process of a gas boiler," *Can. J. Chem. Eng.*, vol. 104, no. 8, pp. 3970–3983, 2026, doi: 10.1002/cjce.70286.
[9] S. Erne, G. Scheger, and W. Wiedemair, "Numerical and experimental investigation of surface-stabilized combustion in a gas-fired condensing boiler," *Results Eng.*, vol. 17, Art. no. 100738, Mar. 2023, doi: 10.1016/j.rineng.2022.100738.
[10] A. Alhashem, A. S. Almutairi, and S. F. Almokmesh, "Flue gas recirculation in steam boilers: A comprehensive assessment strategy for energy optimization and efficiency enhancement," *Processes*, vol. 13, no. 2, Art. no. 395, Feb. 2025, doi: 10.3390/pr13020395.
[11] H. Jiang, L. Lu, X. Gong, Y. Tang, H. Qiu, and Q. Feng, "Influence of excess air coefficient variations on MILD combustion characteristics of CH4/H2 blends and associated NO/CO formation in industrial-scale furnace," *Int. J. Hydrogen Energy*, vol. 204, Art. no. 153304, Jan. 2026, doi: 10.1016/j.ijhydene.2025.153304.
[12] S. Lee et al., "CFD study on combustion and emissions characteristics of methane-hydrogen co-firing in an EV burner," *Case Stud. Therm. Eng.*, vol. 73, Art. no. 106596, Sep. 2025, doi: 10.1016/j.csite.2025.106596.
[13] S. Xu, Z. Tian, Y. Chen, S. Liang, Y. Tu, and H. Liu, "Effect of hydrogen-blending ratio and wall temperature on establishment, NO formation, and heat transfer of hydrogen-enriched methane MILD combustion," *Fuel*, vol. 369, Art. no. 131787, Aug. 2024, doi: 10.1016/j.fuel.2024.131787.
[14] R.-A. Li, R.-Y. Tsai, and Y.-H. Chan, "Thermal–mass transfer and flue gas characteristics of a steam boiler fueled with hydrogen carrier-blended natural gas," *Appl. Therm. Eng.*, vol. 297, Art. no. 130848, Jun. 2026, doi: 10.1016/j.applthermaleng.2026.130848.
[15] O. Salcı and S. Öztuna, "Modeling of hydrogen blending natural gas combustion characteristics and emission analyses in industrial burners," *Int. J. Hydrogen Energy*, vol. 144, pp. 782–797, Jul. 2025, doi: 10.1016/j.ijhydene.2025.03.310.
[16] M. Z. Akram, F. Ma, M. Aziz, Y. Deng, and H. Wu, "H_2 impact on combustion kinetics, soot formation, and NOx emission of hydrocarbon fuel flames," *Fuel*, vol. 338, Art. no. 127321, Apr. 2023, doi: 10.1016/j.fuel.2022.127321.
[17] A. Boretti, "Phased transition from methane to hydrogen in internal combustion engines: Utilizing hythane and direct injection jet ignition for enhanced efficiency and reduced emissions," *Int. J. Hydrogen Energy*, vol. 80, pp. 1255–1265, Aug. 2024, doi: 10.1016/j.ijhydene.2024.07.251.
[18] M. Gore, K. Nonavinakere Vinod, and T. Fang, "Experimental investigation of gaseous mixtures of ethane, methane, and carbon dioxide as an alternative to conventional fuel in spark ignition engines," *J. Energy Resour. Technol.*, vol. 145, no. 3, Art. no. 032301, Mar. 2023, doi: 10.1115/1.4055201.
[19] Y. Kim, B. Y. Park, S. Woo, J. W. Jeong, S. Park, and K. Lee, "Fundamental study for applying a propane gas injection system in a small-ship engine," *Energies*, vol. 16, no. 20, Art. no. 7036, Oct. 2023, doi: 10.3390/en16207036.
[20] A. T. Öztürk, D. Akal, and U. Akyol, "Investigation of the emission values of butane, methane and methane-hydrogen mixtures used in household stove burners," *Int. J. Hydrogen Energy*, vol. 141, pp. 88–98, Jun. 2025, doi: 10.1016/j.ijhydene.2025.05.355.
[21] M. Elkelawy, H. Alm-Eldin Bastawissi, E. A. El Shenawy, M. Taha, H. Panchal, and K. K. Sadasivuni, "Study of performance, combustion, and emissions parameters of DI-diesel engine fueled with algae biodiesel/diesel/n-pentane blends," *Energy Convers. Manag. X*, vol. 10, Art. no. 100058, Jun. 2021, doi: 10.1016/j.ecmx.2020.100058.
[22] M. Çelik, C. Bayındırlı, and R. Kuş, "Experimental investigation of effect of n-hexane addition in diesel and biodiesel fuels on performance and emissions characteristics," *Int. J. Automot. Sci. Technol.*, vol. 7, no. 2, pp. 118–124, Jun. 2023, doi: 10.30939/ijastech.1257614.
[23] K. Lee, J.-M. Kim, B. Yu, C.-E. Lee, and S. Lee, "Effect of various gas compositions on gas interchangeability and combustion characteristics for domestic appliances," *J. Mech. Sci. Technol.*, vol. 27, no. 4, pp. 1191–1201, Apr. 2013, doi: 10.1007/s12206-013-0225-5.
[24] G. Daurer, S. Schwarz, M. Demuth, C. Gaber, and C. Hochenauer, "Experimental and numerical analysis of industrial-type low-swirl combustion of hydrogen enriched natural gas including OH* chemiluminescence imaging," *Int. J. Hydrogen Energy*, vol. 80, pp. 890–906, Aug. 2024, doi: 10.1016/j.ijhydene.2024.07.119.
[25] V. Patel and R. Shah, "Effect of hydrogen enrichment on combustion characteristics of methane swirling and non-swirling inverse diffusion flame," *Int. J. Hydrogen Energy*, vol. 44, no. 52, pp. 28316–28329, Oct. 2019, doi: 10.1016/j.ijhydene.2019.09.076.
[26] Z. Zuo et al., "Combustion characteristics of low calorific value biogas and reaction path of NOx based on sensitivity analysis," *Front. Chem.*, vol. 9, Art. no. 830329, Feb. 2022, doi: 10.3389/fchem.2021.830329.
[27] E. H. Bani-Hani et al., "Optimization of adiabatic flame temperature of natural gas combustion under different conditions," *Environ. Prog. Sustain. Energy*, vol. 43, no. 3, Art. no. e14356, May 2024, doi: 10.1002/ep.14356.
[28] W. Dong, L. Xiang, J. Gao, B. Qiu, and H. Chu, "Effect of CO2 dilution on laminar burning velocities, combustion characteristics and NOx emissions of CH4/air mixtures," *Int. J. Coal Sci. Technol.*, vol. 10, no. 1, Art. no. 72, Dec. 2023, doi: 10.1007/s40789-023-00655-9.
[29] O. A. Marzouk, "Adiabatic flame temperatures for oxy-methane, oxy-hydrogen, air-methane, and air-hydrogen stoichiometric combustion using the NASA CEARUN tool, GRI-Mech 3.0 reaction mechanism, and Cantera Python package," *Eng. Technol. Appl. Sci. Res.*, vol. 13, no. 4, pp. 11437–11444, Aug. 2023, doi: 10.48084/etasr.6132.

[30] I. Yilmaz, Y. Cam, and B. Alabas, "Effect of N2 dilution on combustion instabilities and emissions in biogas flame," *Fuel*, vol. 308, Art. no. 121943, Jan. 2022, doi: 10.1016/j.fuel.2021.121943.
[31] P. Wang et al., "Effects of operating parameters on combustion characteristics of hydrogen-doped natural gas," *Processes*, vol. 13, no. 11, Art. no. 3477, Oct. 2025, doi: 10.3390/pr13113477.
[32] M. Mubashir, D. Shen, H. Kraiem, A. Flah, N. F. Alshammari, and M. M. Hanif, "Machine learning assisted CFD optimization of fuel-staging natural gas burners for enhanced combustion efficiency and reduced NOx emissions," *Sci. Rep.*, vol. 15, no. 1, Art. no. 23547, Jul. 2025, doi: 10.1038/s41598-025-05132-8.
[33] P. J. Swardhamana, N. Ruhyat, and S. Novianto, "Performance evaluation of a condenser at a combined cycle power plant using the LMTD method," *Int. J. Innov. Mech. Eng. Adv. Mater.*, vol. 6, no. 2, pp. 92–100, Sep. 2024, doi: 10.22441/ijimeam.v6i2.27450.